

MASTER SCIENCE DE LA MATIÈRE
École Normale Supérieure de Lyon
Université Claude Bernard Lyon I

Internship 2023
Lucas AOYAGI
M1 Physics

Fermi liquid behavior in twisted bilayer graphene

Abstract : When stacking two layers of graphene and twisting them slightly, we observe in this material (called twisted bilayer graphene), a flattening of the electronic bands of the material which leads to an increase in electron-electron interactions. These enhanced electronic interaction lead to the formation of novel correlated states, such as superconductors or insulators. Here, we chose to investigate the effects of the electronic band flattening on the metallic ground state of twisted bilayer graphene. To do so, we measured the electrical transport properties of 1.4° twisted bilayer graphene down to 1.5K and revealed a ubiquitous Fermi liquid ground state across the flat band. Our observation of the survival of this Fermi liquid behaviour down to very low carrier densities questions the microscopic mechanism of the electron-electron interaction responsible for this metallic state.

Key Words : Twisted bilayer graphene, Metallicity, Fermi liquid, nanofabrication.

Internship supervised by :

Dmitri Efetov

Dmitri.Efetov@lmu.de

Alexandre Jaoui

alexandre.jaoui@lmu.de

Chair of Experimental Solid State Physics - Quantum Materials

Geschwister-Scholl-Platz 1, 80539 München

<https://quantummatter.physik.lmu.de/index.html>



Contents

1	Introduction	1
2	Fermi liquid physics in twisted bilayer graphene	1
2.1	What drives the electrical resistivity of a metal ?	1
2.1.1	Electron-Phonon Scattering	2
2.1.2	Electron-electron scattering	2
2.1.3	Impurity scattering	4
2.2	Twisted bilayer graphene	4
2.2.1	Band structure	4
2.2.2	Within the Fermi liquid picture	5
3	Device Fabrication and characterisation	6
3.1	Fabrication process	6
3.1.1	Exfoliation and Stacking	6
3.1.2	Circuit fabrication	8
3.2	Characterisation methods	9
3.2.1	Raman Spectroscopy	9
3.2.2	Atomic force microscopy	10
4	Experimental setup	11
4.1	Refrigeration system	11
4.2	Resistivity measurements	11
4.2.1	Four-probe method	11
4.2.2	Hall effect	12
4.2.3	Full setup	12
5	Results and discussion	13
5.1	Resistivity for different carrier densities in Twisted Bilayer Graphene Device	13
5.2	Dependence on Magnetic field and Landau fans	14
5.3	Study of the Hall angle in twisted bilayer graphene	14
5.4	Quadratic temperature dependence of the longitudinal resistivity for low carrier densities.	15
5.5	Metallic phase at "magic angle" in twisted bilayer graphene.	16
6	Conclusion	17
	Bibliography	18

Acknowledgements

I would like to thank the group for being so welcoming and allowing me to discover the domain of 2D materials and Twistronics in a very friendly atmosphere. I want to thank Alexandre Jaoui for supervising me during this project and for always being available to answer my questions and Dmitri Efetov for giving me the opportunity to join the group for those three months and giving me the chance to work on this project.

1 Introduction

Single-layer (or few-layers) materials have been heavily studied in the past few decades, especially since the first isolation and observation of graphene by Andre Geim and Konstantin Novoselov in 2004 [1]. Since then, thanks to innovations in fabrication methods [2] [3], many other materials have been successfully isolated as single layers and this has led to a new branch of physics in the study of "2D materials". These 2D materials are particularly interesting as they often have very different properties from their "bulk" counterparts.

Novel fabrication techniques allow for stacking and relative rotation of those single-layer materials, leading to even more new interesting properties. By stacking and twisting these materials, their band structure and thus electrical properties are strongly modified [4]. The study of these modified properties corresponds to the field of "twistronics".

The misalignment of two superimposed graphene monolayers by a small angle (below 2°) (called "twisted bilayer graphene" or TBG) leads to a flattening of the electronic bands near the Fermi level. This band flattening is associated with a strong increase of the electronic interactions in the system, especially for an angle close to 1.1° , the "magic angle", where we see the emergence of exotic phases: superconductors, magnets and, 'strange' metallic phases, which are thought to emerge from these enhanced interactions between electrons [5].

The low temperature behavior of most metals can be described by Landau's theory of Fermi liquid. We wish to study the metallic phase of twisted bilayer graphene (at an angle slightly away from magic angle), in particular, with close attention near the charge neutrality point. This will give us insight on the scattering phenomenon at the origin of resistivity in twisted bilayer graphene.

Here, we report that this metallic phase shows a Fermi liquid behavior for temperatures up to 20K, for doping levels across the entire flat band. In this report, we study the quadratic temperature dependence of the resistivity and wish to understand, within the Fermi liquid picture, the scattering phenomenon explaining this dependence.

Finally, through the measurement of a twisted bilayer graphene device closer to the magic-angle (1.18°) we illustrate the emergence of a metallic regime which is not straightforwardly described by the Fermi liquid theory and reveals signature of 'strange' metallicity.

2 Fermi liquid physics in twisted bilayer graphene

2.1 What drives the electrical resistivity of a metal ?

Resistivity can be described as the ability of a material to limit current flowing through it. A material is more resistive if electrons flowing through it lose momentum through scattering events. The simpler model to describe resistivity in metals is the Drude model. The Drude model consists in describing a metal as a free electron gas undergoing collisions with "defects" of the crystalline structure of that metal at a rate τ . The model, however simple, qualitatively describes well a number of materials for large ranges of temperature and recovers Ohm's law.

For most metals, we can distinguish different regimes corresponding to different scattering processes with different scattering rates τ .

2.1.1 Electron-Phonon Scattering

At high temperature, the "defects" mentioned previously in the context of the Drude model are the vibrational modes of the lattice, phonons. The source of resistivity is thus electron-phonon scattering.

The phonon density in metals follows the Bose distribution.

$$n(\omega) = \frac{1}{e^{-\frac{\hbar\omega}{k_B T}} - 1} \underset{T \gg \Theta_D}{\approx} \frac{k_B T}{\hbar\omega} \quad (1)$$

which in the high temperature limit is linear in temperature. This gives a linear in temperature scattering rate $\frac{1}{\tau}$ [6] and thus linear in temperature resistivity. The high temperature limit being defined by the Debye temperature $\Theta_D = \frac{\hbar\omega_D}{k_B} = \frac{\hbar q_D v_q}{k_B}$, with v_q the velocity of sound in the metal and q_D can be seen as the range of accessible vectors for scattering in k-space.

For temperatures lower than the Debye temperature, the resistivity due to electron-phonon scattering is no longer linear but proportional to T^5 because scattering events corresponding to smaller wave vectors \mathbf{q} are then favored. As the temperature is lowered below the Debye temperature, electron-phonon collisions are suppressed until eventually this contribution becomes negligible to the material resistivity. At sufficiently low temperature, another sources of inelastic scattering can dominate: electron-electron scattering.

2.1.2 Electron-electron scattering

At lower temperatures, phonons become less important and the metallic regime can be dominated by electron-electron scattering. In this context, electrons in a metal form an ensemble of fermions in interaction which, under certain assumptions, can be described as a Fermi liquid. Even though it was first proposed to describe the behavior of Helium 3, most metals can be described by the Fermi liquid picture [7].

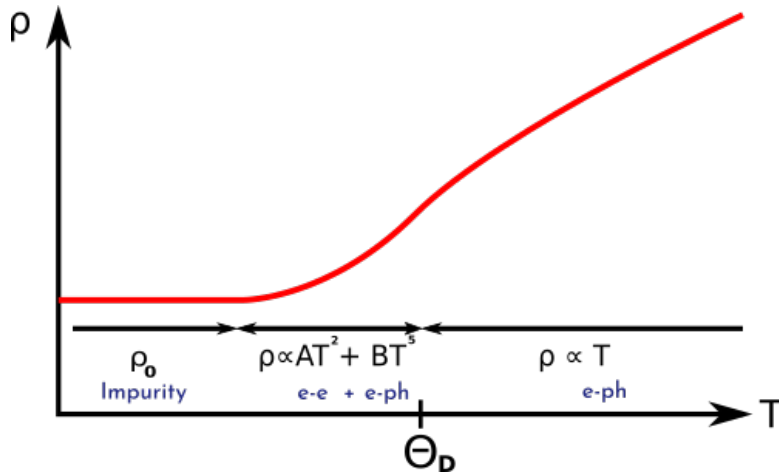


Figure 1: Typical Resistance as a function of Temperature curve for 3D metals

The core idea of the Fermi liquid picture is the introduction of quasi-particles, of effective mass m^* and of lifetime τ_k , to account for the interactions (introduced adiabatically in the non-interacting system). However, we make the assumption of low interaction strengths and of the absence of induced phase transitions.

Because of Pauli's exclusion principle, interacting electrons can only scatter to empty states and thus only electrons in a thin shell around the Fermi surface will take part in the scattering process. In the low energy limit, this shell is of radius $k_B T$. If we consider the Fermi surface to be the surface of a sphere of radius k_F (with k_F the Fermi wave-vector), the probability of finding two such electrons for the scattering process is thus proportional to $\frac{k_B^2}{k_F^2} T^2$. We thus expect the resistivity of a Fermi

liquid to have a quadratic dependence in temperature. We can note that the resistivity contribution of the electron-electron scattering process is inversely proportional to the square of k_F and thus inversely proportional to the Fermi energy. Metals with high Fermi energies will thus have a low electron-electron scattering contribution. This is why the T^2 resistance at low temperature is hardly ever reported in typical metals such as Cu, Al, Ag..

However, the scattering processes explaining the origin of resistivity in those systems are not always well understood. Indeed, when electrons scatter with each others, the law of momentum conservation should imply that the momentum stays in the electron system and thus this should not induce any resistivity. The momentum still has to "leak" to the lattice. Two processes can explain increased resistivity by scattering between electrons in the Fermi liquid picture.

Umklapp scattering [8] can explain a "non-conservation" of momentum in periodic crystals. In a periodic lattice, electron momentum is only conserved up to one reciprocal lattice vector. Indeed, any wave vector outside of the first Brillouin zone can be expressed as a vector inside of the Brillouin zone, this allows for scattering that doesn't conserve the crystal momentum, by relaxing a lattice vector. This allows two electrons to scatter in the same direction for instance (see Fig.2). In Umklapp scattering the momentum difference between incoming and outgoing electrons is equal to any integer number times the unit vector \mathbf{q} of the reciprocal lattice [9].

$$n\vec{q} = \vec{k}_{1f} + \vec{k}_{2f} - \vec{k}_{1i} - \vec{k}_{2i} \quad (2)$$

with $k_{ji/f}$ the wave vector of the photon j before or after the scattering event and $n \in \mathbb{Z}$. To observe this phenomenon, we thus need the norm of the Fermi wave vector (equal to the norms of $k_{ji/f}$) to be larger or equal than a quarter of the Brillouin zone width (the norm of \mathbf{q}). To express this condition we make here the assumption of a rather "simple" Fermi surface.

$$k_F \geq \frac{1}{4} \|\vec{q}\| \quad \text{with} \quad k_F = \frac{\sqrt{2m^*E_F}}{\hbar} \quad (3)$$

The second way to explain resistivity induced by scattering between electrons is to have a multi band pocket electronic system [8], as proposed by Baber in 1937 [10]. This was originally proposed to describe transition metals, but the two band system can in practice be applied to many materials and in particular to Twisted bilayer graphene.

The two bands carry electrons with different effective masses. Assuming we have two electrons of charge e and of respective effective masses m_1^* and m_2^* of initial wave vectors \vec{k}_{1i} and \vec{k}_{2i} and final, after scattering, \vec{k}_{1f} and \vec{k}_{2f} . The conservation of momentum implies $\vec{k}_{1i} - \vec{k}_{1f} + \vec{k}_{2i} - \vec{k}_{2f} = \vec{0}$. The variation in current can be written as (cf [10]).

$$\Delta\vec{j} = e\hbar\left(\frac{1}{m_1^*} - \frac{1}{m_2^*}\right)(\vec{k}_{1i} - \vec{k}_{1f}) \quad (4)$$

The variation in current, which leaks to the lattice, scales with the difference in the effective mass of electrons from the two distinct bands. In a two-band model, with a strong difference in effective mass between the two bands, Baber scattering can explain a rise in resistivity from a scattering between two electrons.

Depending on the Fermi energy, we can also have scattering between electrons and holes, in which case $e_1 = -e_2$, in this case the variation in current also scales with the difference in effective mass. In both cases, without a strong effective mass difference Baber scattering is negligible compared to other scattering processes.

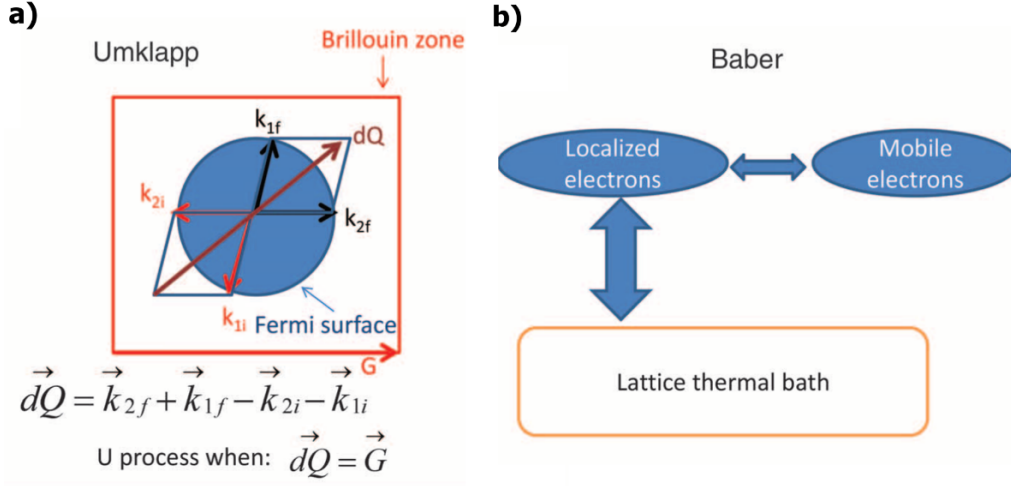


Figure 2: a) Scheme representing the principle of Umklapp Scattering b) Scheme representing the principle of Interband Exchange Scheme (both Figures taken from [9].)

2.1.3 Impurity scattering

At even lower temperatures, electron-electron scattering becomes negligible compared to the scattering with impurities. Impurity scattering gives a scattering rate constant with regard to temperature and contributes to a "base" resistivity R_0 at $T=0$. However, for most metals, R_0 can be important compared to electron-electron scattering for a larger range of temperatures, hiding the Fermi liquid behavior at low temperatures before it is hidden by electron-phonon scattering at higher temperatures. This makes the observation of this behavior complicated in many systems. However, twisted bilayer graphene, being a system where electrons interact a lot, with a low Fermi energy, and with a low R_0 due to impurities, is an ideal material to observe the Fermi liquid regime.

2.2 Twisted bilayer graphene

2.2.1 Band structure

The material we will study is "twisted bilayer graphene" and is represented schematically in Fig.3. It is composed of two graphene layers twisted with respect to one another. For low angles, the band structure of twisted bilayer graphene becomes very different from that of graphene (represented in Fig.4). Graphene's band structure is characterised by a linear dispersion around the Fermi level (Dirac bands). Around the Dirac point, electrons move very fast making graphene a ultra-high mobility metal. However, in the case of Twisted bilayer graphene, the bands from the two layers of graphene hybridize and for angles close to 1° a flat band appears around charge neutrality, separated from higher energy bands by a gap [11].

The electrons in the flat band (represented in Fig.4) have very low kinetic energy. This means that, in comparison, the potential energy, the interaction between electrons is no longer negligible. Twisted bilayer graphene can be labelled as a "strongly correlated system", a system in which interactions between electrons can no longer be omitted.

The formation of the flat band is directly linked to the formation of a "Moiré", a geometrical pattern created by the superposition of the two layers. As we see in Fig.3, in some regions (lighter in the image), carbon atoms from the two different layers are directly above one another, the material is locally in the AA configuration. In other regions (which appear darker in the image), carbon atoms are in the AB configuration. This changes the periodicity of the material (the size of the unit cell), which thus also changes the size of the Brillouin zone. Indeed, with scanning tunneling microscopy for instance one can see that electrons seem to concentrate in the AA regions [4], leaving the AB regions rather empty. The delocalization of electrons in k-space because of the flat-band results in the localisation

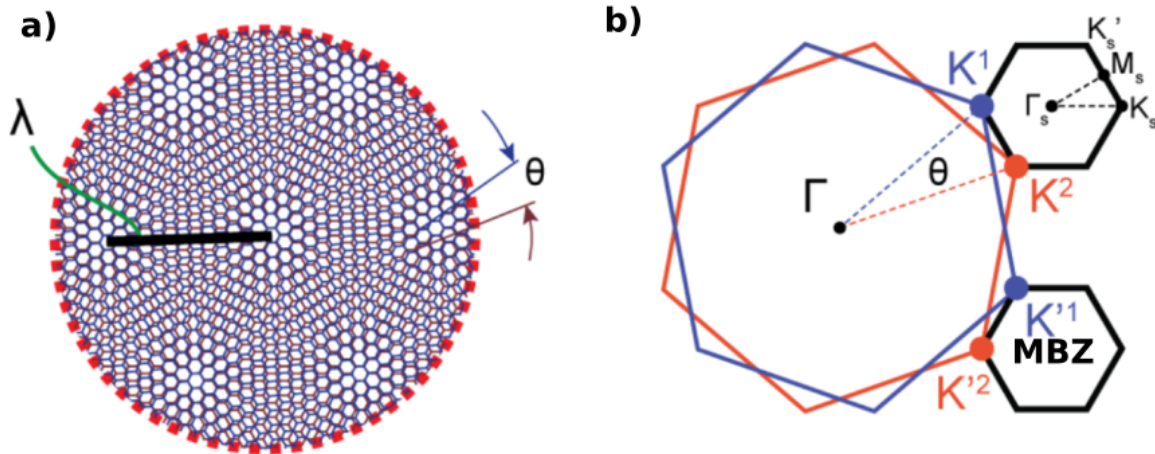


Figure 3: a) Schematic representation of twisted bilayer graphene with a moiré pattern b) Schematic representation of the Brillouin zone of Twisted bilayer graphene. (both figures taken from [11])

of electrons in real-space. This leads us to consider a new "superlattice", with a much larger lattice constant (around 10 nm for angles close to 1° , against 0.2 nm for graphene). This is transposed in \mathbf{k} -space by the creation of "mini-Brillouin zones" or in the band structure with "mini-bands". The electronic properties of the material are heavily influenced by these new formed bands.

For twist angles close to a certain value of 1.1° , called the "magic angle", electron correlations lead to many new interesting phases of matter such as superconductivity, strange metal or correlated insulator phases.

2.2.2 Within the Fermi liquid picture

A quadratic temperature dependence of resistivity has been reported in twisted bilayer graphene [13] and in graphene/hexagonal Boron Nitride moirés [14]. We will try to understand this behavior within the Fermi liquid picture. As explained in Sec.2.1.2, in the Fermi liquid model two phenomenons can explain the T^2 resistivity dependence, Umklapp scattering or Baber scattering.

However, for Umklapp scattering [14], we need a large Fermi surface to satisfy the condition $k_F \geq \frac{1}{4} \|\vec{q}\|$. This can be transposed into a condition on the carrier density.

$$n \geq \frac{\pi}{4a^2} \quad (5)$$

With n the carrier density and a the lattice constant (the lattice constant of the superlattice since we consider the Umklapp scattering within the mini-Brillouin zone). We can estimate the lattice constant of the superlattice, $a \simeq a_0/(2 \sin \theta/2)$, with a_0 the lattice constant of graphene and θ the twist angle.

With $a_0 = 0.25$ nm and with a small angle of around $\theta \simeq 1.35^\circ$ we find $a \simeq 10$ nm. For twisted bilayer graphene, the conditions for Umklapp scattering are $n \geq 7 \times 10^{11} \text{cm}^{-2}$ (Note that half filling of the band for twisted bilayer graphene is around $2 \times 10^{12} \text{cm}^{-2}$).

Baber scattering does not need assumptions over the size of the Fermi surface. In the case of twisted bilayer graphene, theoretical propositions have been made as to the nature of these two separate bands. Some suggest that we can distinguish two types of electrons, heavy (in effective mass) localized electrons and delocalized mobile electrons [15].

With electrical transport measurements as a function of temperature outside of the Umklapp scattering conditions, we can try to isolate the phenomena behind resistivity at low temperature in twisted bilayer graphene.

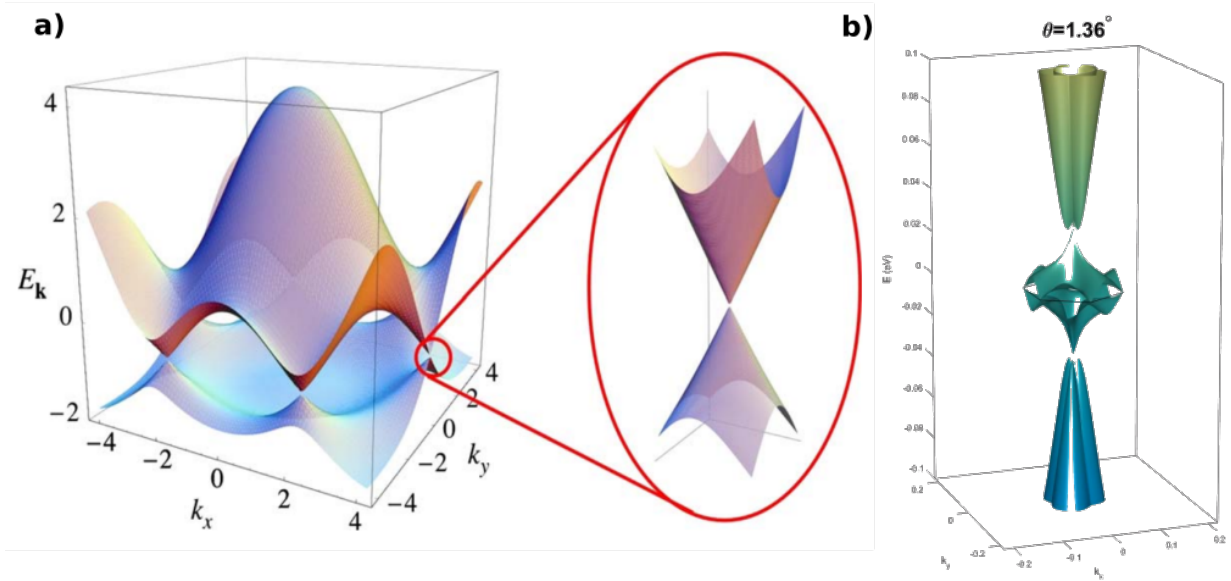


Figure 4: a) Band structure of graphene and Dirac cone in the low energy limit in the inset (Figure taken from [12]) b) Band structure of twisted bilayer graphene in the low energy limit for an angle of 1.36° using the continuum model (taken from [5] (Supplementary Material)).

3 Device Fabrication and characterisation

3.1 Fabrication process

Before reporting the experimental results on the electrical transport properties of twisted bilayer graphene, I will describe here the various steps of fabrication and initial characterization of this material that I have discovered along this internship. From start to finish, the process to fabricate a device ready for measurement is quite lengthy and making a twisted bilayer device close to magic angle is especially complicated. Indeed, twisted bilayer graphene is in a meta-stable state and for such low angles the device can easily relax back to the more stable orientation of a 0° angle, making the yield of the fabrication process quite low. Which is why the device I measured was fabricated by Roop K. Mech, a PhD student of the group. However I still learned several fabrication steps, which are detailed in this section.

The fabrication process consists in making a "stack" (also called hetero-structure), a superposition of different materials serving different purposes. The stack is composed of a "gate" to change the carrier density in the material, a dielectric insulating layer, the material we wish to study and another dielectric insulating layer. The insulating layer serves multiple purposes, it keeps the gate from "leaking" current into the material, it also changes the carrier "mobility" of the material (the speed of the electrons when the material is under an electrical field).

3.1.1 Exfoliation and Stacking

The first step in twisted bilayer graphene device fabrication is to isolate the different elements which we will stack into our hetero-structure.

We need a **thin layer of graphite** (around 10 nm in thickness) which will serve as the gate to sweep the carrier density by acting as a field effect transistor. When we place an insulating layer in between of the gate and the twisted bilayer graphene, a simple change in voltage to the gate changes the

electron or hole doping in the twisted bilayer graphene. This allows us to sweep the Fermi energy over a large range by simply changing a voltage. This tuning knob is one of the reason why 2D materials are so interesting to study. For 3D materials such as cuprates (copper oxides) for instance, in order to reach the whole phase space and measure different carrier density, one would need to fabricate a new device with different electron/hole doping each time [16].

We also need **two thin layers of hexagonal Boron Nitride or hBN** (around 10 nm in thickness) to serve as a dielectric insulating substrate to encapsulate the twisted bilayer graphene. In order to make quality devices, a good substrate is essential. The substrate needs to have a smooth surface, be a good dielectric (an insulator that can be polarized when subjected to an external electric field), have a low defect density and be somewhat geometrically compatible with the hetero-structure (have a similar lattice constant for instance). hBN is a great candidate for a good substrate for device fabrication. Devices made with hBN rather than SiO_2 as substrate show much better carrier mobility and much less defects [17].

Finally, we need **graphene**, in order to fabricate the twisted bilayer graphene, the material which we want to study.

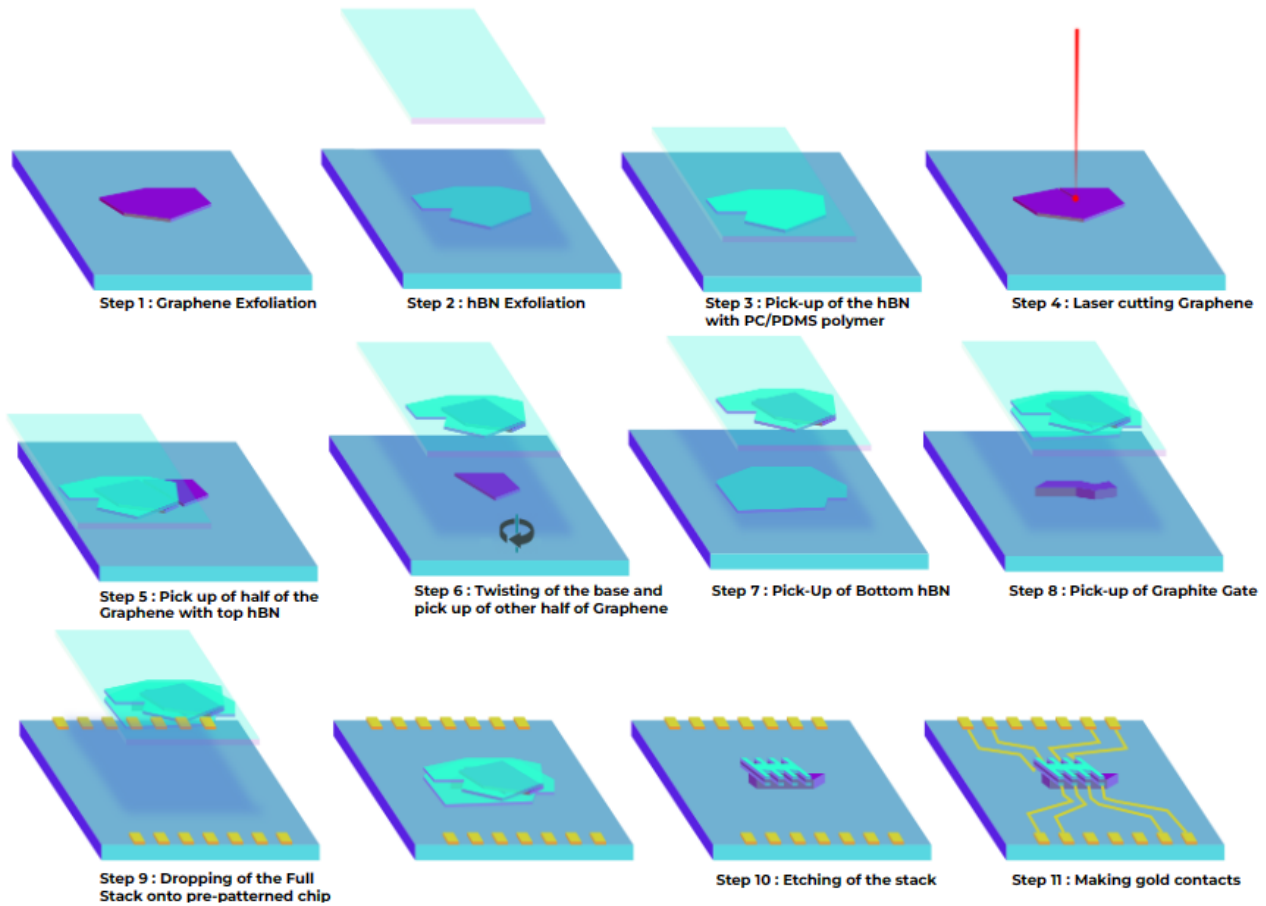


Figure 5: Complete scheme of the exfoliation, stacking, and hall bar fabrication process (with pictures)

The method most commonly used is mechanical exfoliation with scotch tape and is the one used in the group (other methods such as Chemical Vapour Deposition [18] can be used, however, it is more complicated to put in place and less adapted to our usage). The idea is to use the stronger adhesive power between the tape and graphene (or hBN) layers than the one between the different layers of graphene (or hBN) in the bulk graphite (or hBN).

We then put the tape with which we exfoliated down onto a substrate (a silicon chip with a thin layer of SiO_2 of 290 nm in thickness on top), which we etched with a plasma in order to make it more

adhesive. We also heat up for a few minutes the tape with chips stuck to it (before removing the chips from the tape) which releases gas from the interface. The pressure difference obtained after cooling down the tape to room temperature also increases the Van der Waals forces at the tape/graphene interface. [3]

We now have a Si chip with different thicknesses of exfoliated graphite on top, including monolayer graphene. We do the same process to exfoliate the hBN.

We are now ready to stack the different layers one on top of the other. The stack is composed of a top graphite gate, a top hBN, our twisted bilayer graphene, a bottom hBN and a bottom graphite gate.

The whole stacking process is represented in Fig.5. In order to pick up the different few-layers materials, we use a polymer (PC - Polybisphenol A carbonate with PDMS - polydimethylsiloxane) which has a good adhesion to the material (better than the Silicon Oxide) at room temperature but has a weak adhesion when heated up, so that we can release the material.

To stack the twisted bilayer graphene, we start with one graphene flake which we cut in half with a laser of frequency $f = 1048 \text{ nm}$ (where graphene absorbs well) and then stack one half onto the other. A new method currently being implemented in the group is Atomic Force Microscopy anodic cutting, by using an AFM with a conductive tip and putting a voltage on the tip, the water in the air will react with the graphene next to the tip where the voltage is applied in order to burn away the graphene, which also gives quite clean cuts [19].

Step 9 is the last step of the stacking process in which the full stack is dropped onto a chip with pre patterned gold contacts.

3.1.2 Circuit fabrication

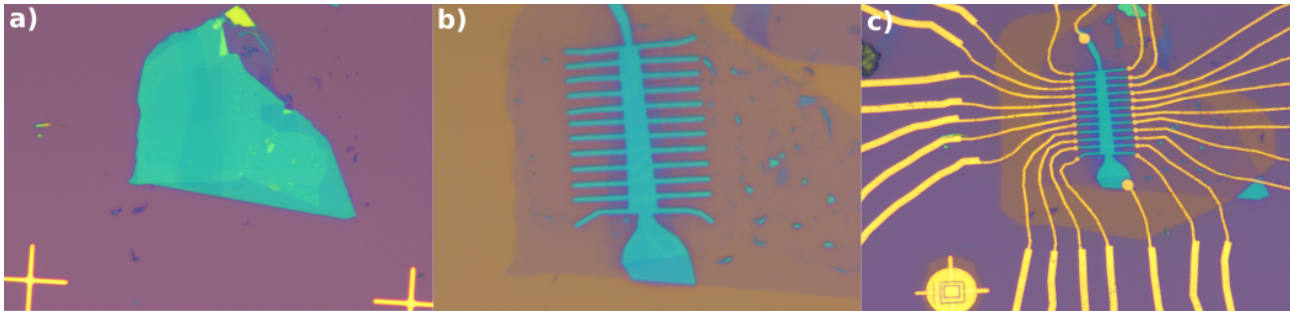


Figure 6: Optical Microscope Image of the stack at different steps. a) Full stack (After Step 9 in Fig.5) b) After etching of the Hall bar (Step 10 of Fig.5) c) After evaporation of gold and chromium for contacts. (Step 11 of Fig.5)

Learning the lithography and evaporation steps (Steps 11 and 12 on Fig.5) can be a lengthy process, I did not perform these steps myself, I will thus only briefly explain these nonetheless important fabrication steps.

In order to measure electrical transport properties in the stack, we need to make a "Hall bar" (the reason behind the Hall resistivity measurements is explained in Sec.4.2.1, as is the working principle of the "four-probe" resistivity measurements).

First, we etch the stack into the shape of an Hall bar, by first making a mask with a polymer resistant to the etching (950A2 PMMA) (the polymer mask is made into the shape of an Hall Bar with electron beam lithography). We then etch away the part of the stack not protected by the mask with a Ar/O_2 plasma, before cleaning with MIBK/IPA 1:3 and acetone. We are left with a stack in the shape of a Hall bar (See Fig.6).

We then make another polymer mask leaving exposed only the area on which we make the contacts. We then evaporate 5 nm of chromium (better adhesion to the silicon oxide substrate) and 50 nm of gold. Before removing the mask and the metal evaporated over the mask in acetone. In Fig.6, we show some optical microscope images of the stack at different corresponding steps.

Note that many regularly spaced contacts are made on the device. Indeed, Twisted bilayer devices can be quite inhomogeneous in angle (different regions of the sample have different angles and thus can have different properties. This is why we want to be able to measure electrical transport locally on the device.

3.2 Characterisation methods

It's very useful to characterise the sample during the different fabrication steps, whether it is before stacking to select a good graphene flake or after fabrication for imaging of the device.

3.2.1 Raman Spectroscopy

I spent part of my Internship learning how to characterise graphene on a Raman microscope (Witec Alpha300 apyron) recently acquired by the group. Raman Spectroscopy is a technique used to determine the vibrational modes of a material. It is based on the inelastic scattering of photons by phonons, which are the vibrational modes of the material [20]. When sending a photon on a material, different phenomena can occur. The most probable one is the elastic scattering of the photon (called Rayleigh scattering), it occurs when the system goes to a higher energy due to the incoming photon and then goes back to the initial state releasing a photon of the same energy as the incoming one. The other scattering event that can happen is Raman Scattering. Different types of Raman scattering can happen, for instance, when a photon loses part of its energy in the interaction process, the system can end up in a higher energy vibrational mode (Stokes process). If the photon finds the system in a vibrational mode, it can leave the interaction with higher energy and bring down the system to its ground state (Anti-Stokes). If the incoming photon has an energy corresponding to an excitation energy of the system, it's called resonant Stokes (or Anti-Stokes scattering). Usually, Raman Spectroscopy corresponds to Stokes measurements (as they are much more probable than Anti-Stokes) and give the intensity of the scattered light as a function of the wavelength (or equivalently as a function of the difference between the incoming photon's energy and the scattered photon's energy (in cm^{-1})). On a Raman spectra, we will observe different peaks at wavenumbers corresponding to transition energies of vibrational modes (see Fig.7.a)).

In a Raman microscope, we send photons of specific frequency (here $\lambda = 532 \text{ nm}$) to excite the sample. The reflected and scattered light then goes through a spectrometer to separate the different frequencies. The intensities of the different frequencies are then measured by photodiodes.

This technique can be used to characterise many of the properties of graphene. We can first characterise the **number of layers** of graphene. Indeed, the G peak's (corresponding to the in-plane phonon E_{2g}) intensity scales with the number of layers [21]. In Fig.7.b), we show a map of a flake obtained by taking the integrated area of the G peak for each pixel.

We can also characterise **defects** in a sample which could otherwise not be seen with an optical microscope. This can be particularly useful as defects in the sample can cause problem later in the stacking problem (they can create bubbles, and the defects can expand during the fabrication process). Indeed, the D mode (corresponding to the "breathing modes" of the lattice) is sensitive to defects as it is activated by translational symmetry breaking. The D peak will thus be observed around defects and edges [20]. In Fig.7.c) we show a map obtained by integration of the D peak. We can see that it is only visible at edges and defects. Note that the D peak is dependent on polarisation and is maximum when the polarisation of the incoming light is parallel to the defects.

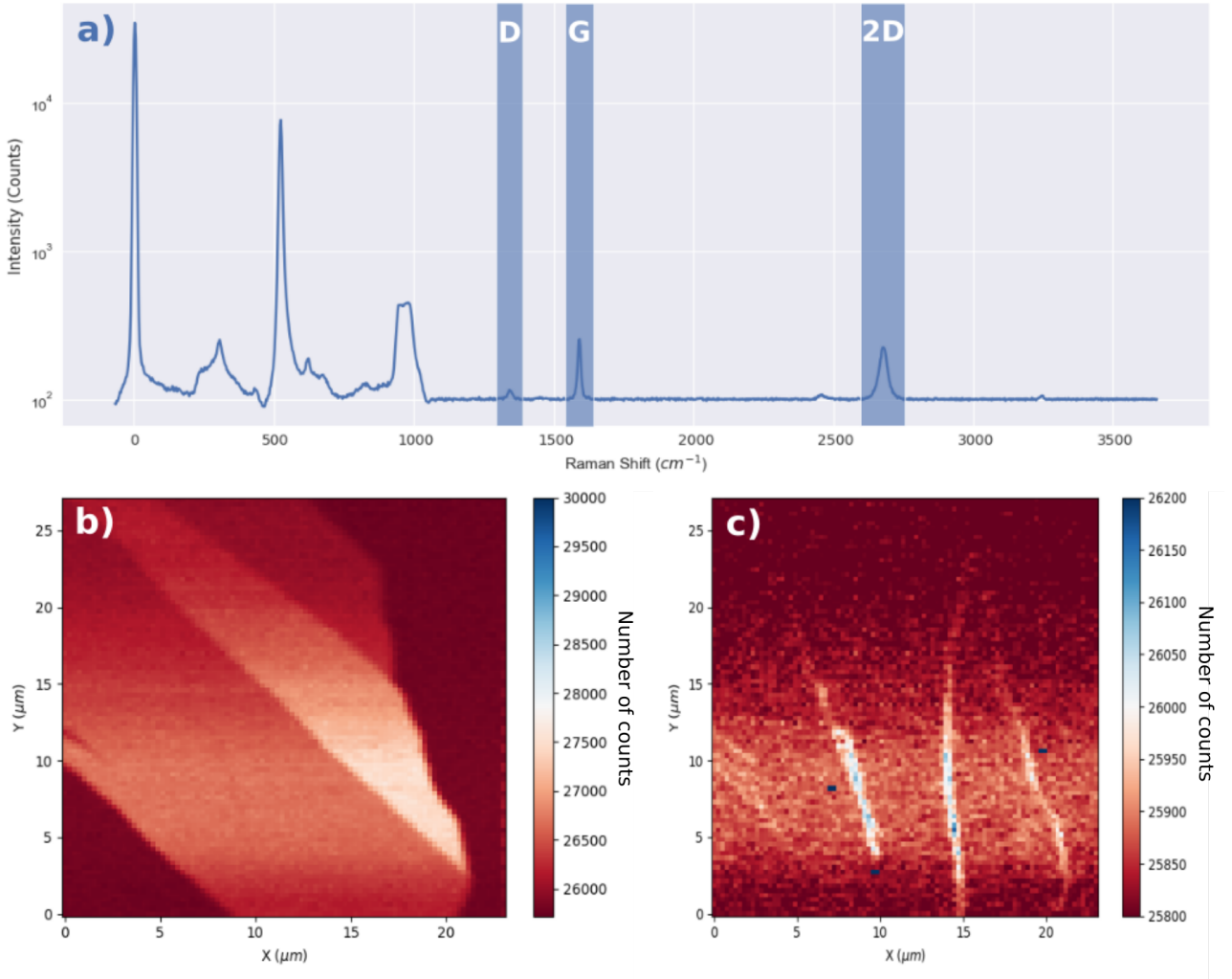


Figure 7: a) Raman Spectra taken at the edge of a monolayer graphene flake with notable modes highlighted (at 0 cm^{-1} , we see the Rayleigh peak, the peaks below 1000 cm^{-1} correspond to the silicon substrate) b) Map obtained through the integrated area of the G peak c) Map obtained through the integrated area of the D peak for the same flake.

We can also characterise **strain** in the lattice thanks to Raman microscopy, which is also useful during the stacking process as strain can lead to the relaxation of the twisted bilayer graphene, or bigger inhomogeneities in angle over the flake. In order to do this, we can map the G mode which undergoes a doubling of the peak when the flake is strained [22]. Raman Spectroscopy can also allow us to identify the crystallographic axis of a flake [23].

Remark : During the internship, I also studied other useful applications of Raman microscopy on other graphene related materials, such as ABA and ABC stacked trilayer graphene. ABC trilayer graphene having many interesting properties such as a flat band in its electronic structure, under large displacement fields, and showing superconductivity at low temperature [24].

3.2.2 Atomic force microscopy

I also, during this internship, learned to use an Atomic force microscope. Atomic Force Microscopy [25] is a precise local probe microscopy. A tip is placed on the edge of a cantilever, (in the "tapping mode" which we use) the cantilever moves in a sinusoidal motion at its resonant frequency, when the tip is interacting with the sample, the motion of the cantilever is going to be modified (its amplitude). This change is measured thanks to a laser reflecting on the surface of the cantilever. The reflected

light goes to photodiodes, the amount of light reflected to those photodiodes depends on the position and motion of the cantilever. A schematic representation of the working principle of an AFM is given in Fig.8.a).

The AFM is the most precise imaging method in the lab. It is often used to get high quality images of the device. An AFM image of the device is shown in Fig.8.b). We can from this image also extract the thickness of the hBN layer, which is useful as different thickness can have different effect on the mobility of electrons and influence the effect of the gate.

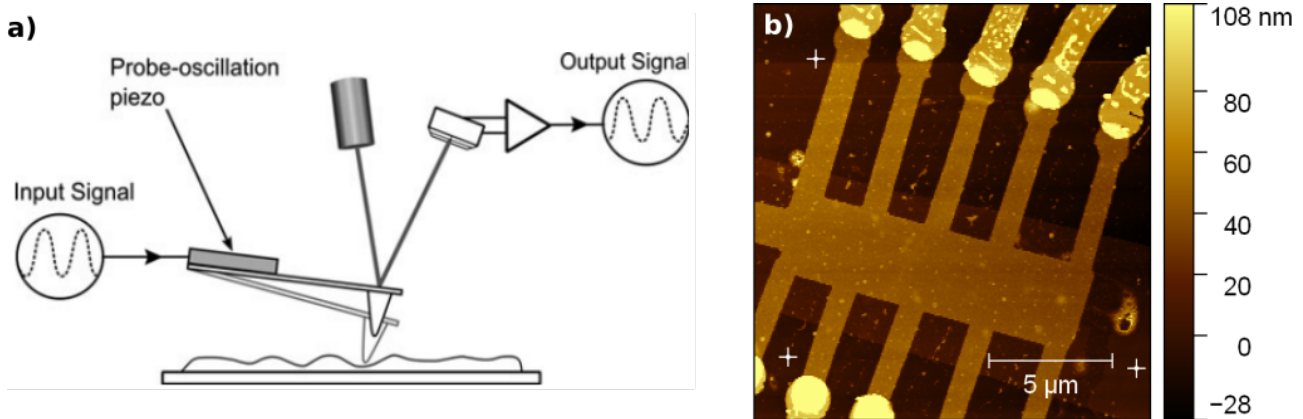


Figure 8: a) Scheme of the working principle of Atomic Force Microscopy (taken from [25]) b) Image of a full device obtained by Atomic Force Microscopy in tapping mode

It can also be used during the stacking process, indeed, before stacking the graphene onto the hBN we might want to make sure that the hBN has a smooth and flat surface with no defects (indeed, the hBN is quite thick and small changes in thickness might not be visible with an optical microscope). Defects or "dirts" on the hBN might create bubbles later in the stack which can then create important inhomogeneities in angle.

4 Experimental setup

In this section, we detail the experimental setup used to measure electrical transport in a twisted bilayer graphene device.

4.1 Refrigeration system

Electronic interactions dominate the system in the degenerate regime, i.e. when $T \ll T_F$, which imposes to study TBG at low temperatures. We use for this purpose a variable temperature insert, produced by "Ice Oxford", with a base temperature of 1.5K and equipped with a 8T unidirectional magnet.

The fridge works with a closed cycle of Helium 4 in gas form and with a compressor. Cold low pressure gaseous Helium 4 is put into the chamber with a needle valve, the gas takes heat from the chamber, is then compressed and exchanges heat with another disconnected cryogenic cycle. The gas is then relaxed to low pressure (around a few millibar) before being put back into the chamber. The system is called "dry", but when the chamber reaches 4.2K, the Helium 4 then liquefies during the heat exchange with the chamber. The system can reach a minimum temperature of 1.5K.

4.2 Resistivity measurements

4.2.1 Four-probe method

The four point probe resistivity measurement allows us to bypass the resistance of the probing system. Two outer probes circulate the current I , while two inner other probes measure a voltage. Since the

voltmeter has a high impedance, no current circulates in the two inner probes, the measurement doesn't take into account their resistivity. We only measure the resistivity of the material in between the two voltage probes.

The contacts used for the measurement of both the longitudinal resistivity and of the transversal one (when a magnetic field is applied) are represented in Fig.9.

4.2.2 Hall effect

When we apply a magnetic field orthogonal to a 2D material with a current circulating, the Lorentz forces change the trajectory of the charges going through the material. This creates an accumulation of charges on one side of the material, creating a difference of potential and an electric field going against the direction of the Lorentz force, thus establishing a stable electric potential. We call "Hall resistance", the newly introduced resistance in the transversal direction. Measuring the transversal resistivity when the system is under a magnetic field gives very useful information on the system. Since we measure at low temperature on an almost 2D system, we also measure some features of the Quantum Hall effect. At low temperatures and high magnetic field, the electrons take circular "cyclotron" orbits which are quantized in "Landau levels".

Measuring the Hall resistivity and Landau levels can give us useful information on our device such as the carrier density for instance.

4.2.3 Full setup

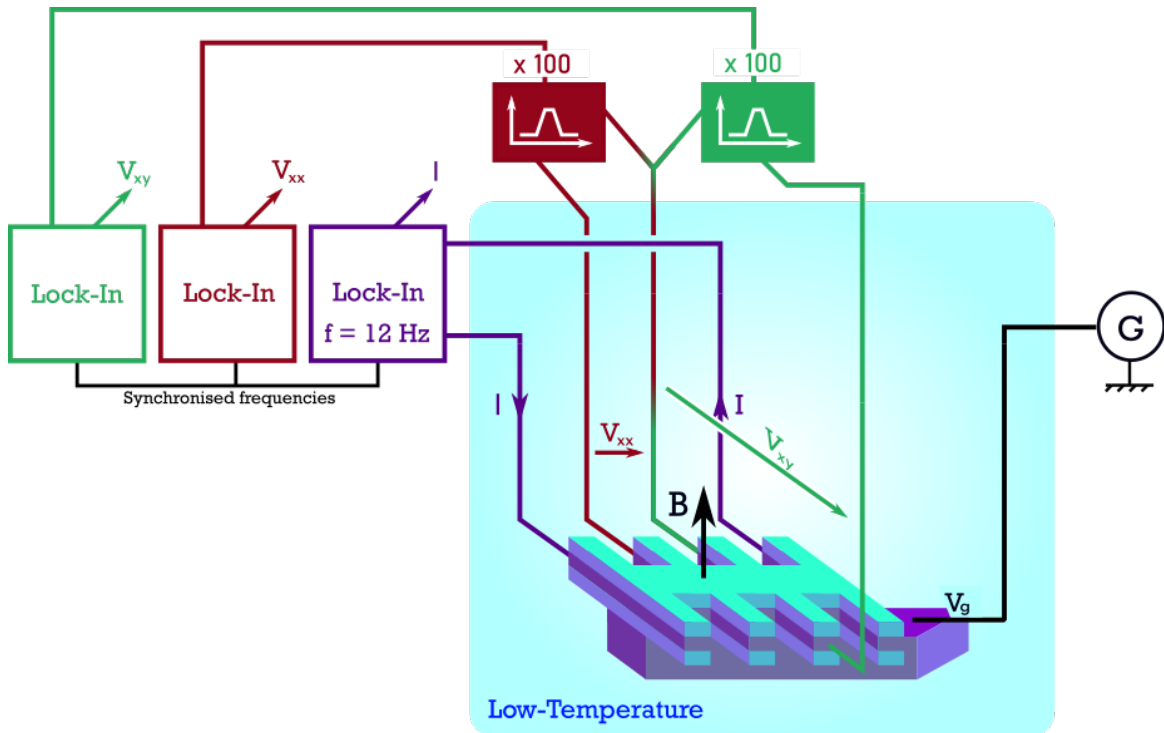


Figure 9: Full experimental setup of measurements.

In Fig.9, we show a detailed scheme of the experimental setup. The contacts on the device are explained in the previous section. All of our voltage and current measurements are made using the Lock-In method. We send our current I at a certain frequency (here $f = 12.25$ Hz, the choice of frequency is made to limit some ranges of noise and we also want to make sure to use a frequency not used for any other measurement in the lab to avoid parasitic signals), the lock-in isolates that specific frequency in the signal measured on the device. We measure both the in-phase signal (at

frequency f) and the out of phase signal (at all other frequencies). We use the Lock-in for the current measurement, the longitudinal and the transversal voltages. The lock-in method allows us to remove from our measurement noise having a different frequency than the one used to send in the signal, and thus largely removes white noise (constant for all frequencies) or $1/f$ noise.

The measured voltages V_{xx} and V_{xy} also go through a Stanford Instrument pre-amplifier with integrated filter. This allows us to get a higher signal to noise ratio.

When handling the contacts, we need to be very careful. Indeed, if we are not at the same potential as the ground of the setup, we might create an electrostatic discharge which will destroy the device. When changing contacts we thus put on a bracelet putting us at the ground potential of the measurement.

We have now seen the different aspects of device fabrication and the technical aspects of transport measurement, in the next section, we show some transport measurement giving us insight on the Fermi liquid behavior of the metallic phase of our twisted bilayer graphene device.

5 Results and discussion

5.1 Resistivity for different carrier densities in Twisted Bilayer Graphene Device

The device we studied is slightly above the "magic angle" of 1.1° as we want to study the metallic phase and not the more complex phases arising closer to the magic angle. Here, in Fig.10, we show at zero magnetic field the resistance as a function of carrier density for a temperature of 1.5 K. On this plot we can distinguish two interesting phases. At the center of the plot we see the charge neutrality point where the electron/hole density reaches zero, this phase is characterised by a highly resistive state. At the extremities of the plot, we see the band insulators corresponding to the gap between the flat band and the dispersive bands (cf. Fig.4). These band insulators are a direct feature of the flat bands, as they show a separation of the graphene's Dirac bands into a middle flat band and two more dispersive (less flat, where electrons have a much higher mobility).

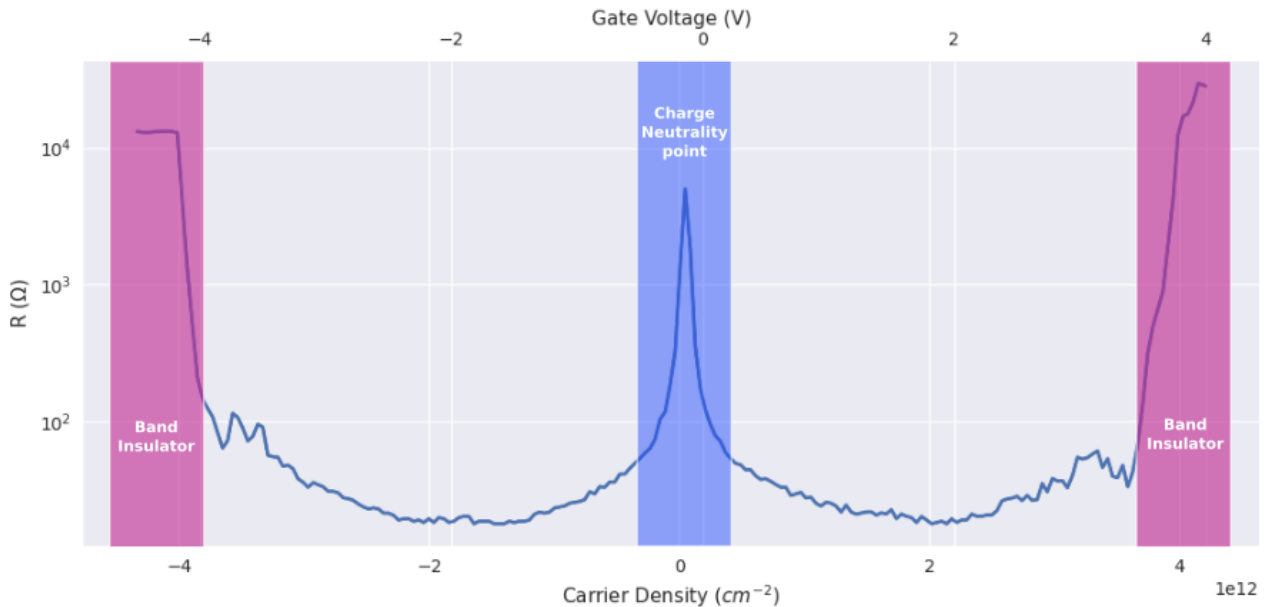


Figure 10: Resistivity as a function of electron doping for a device at 1.33° and identification of notable phases at 1.5K.

In this report, we're particularly interested in the metallic phase located around charge neutrality.

5.2 Dependence on Magnetic field and Landau fans

Here, in Fig.11 a), we report the Hall resistance of the device as a function of magnetic field for B between 0 and 2 T, for a gate voltage $V_g = 1.30V$.

From this measurement, we can extract the carrier density at each gate voltage (reminder, the gate voltage is proportional to the carrier density), we can repeat this procedure for successive gate voltages to map the carrier density. For a gate voltage V, we can from the curve of R_{xy} as a function of B extract the carrier density at this gate voltage V, n_V (see Eq.6). By extracting the slope of $R_{xy} = f(B)$, we obtain $\frac{1}{en_V}$ and we can then easily extract n_V . We measure at low field to avoid non-linear effects.

$$n_V = \frac{B}{eR_{xy}} \quad (6)$$

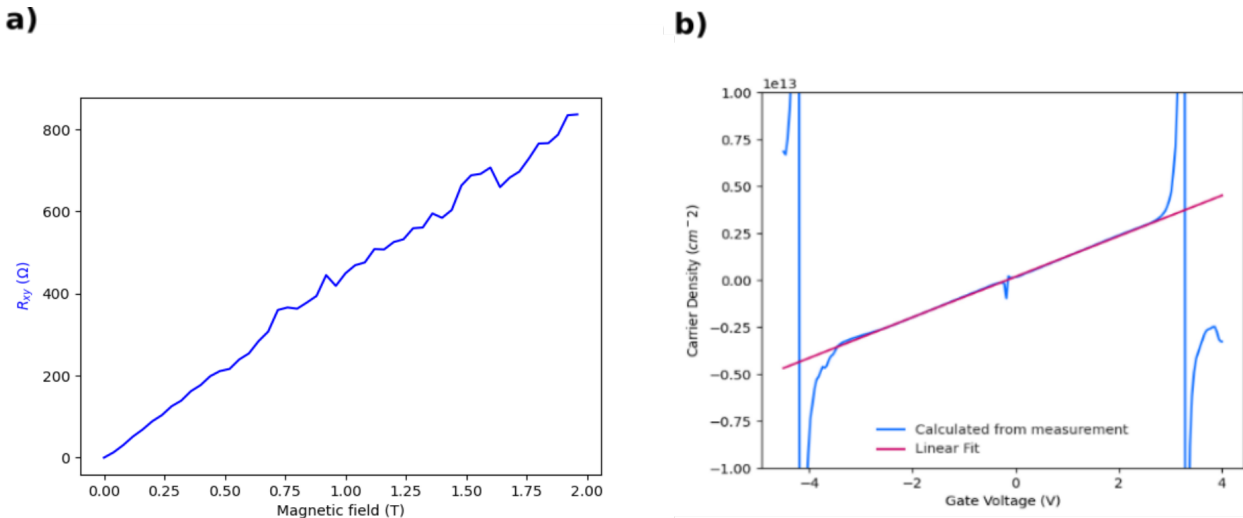


Figure 11: a) Plot of the Hall resistance R_{xy} and of the longitudinal resistance R_{xx} as a function of magnetic field between 0 and 2 T at 1.5K for $V_g = 1.30V$ b) Carrier density as a function of gate voltage

We show in Fig.11 b) the carrier density as a function of gate voltage. We can see that this calculation of the carrier density is not accurate anymore at the insulating states at charge neutrality or at the extremities of the band. We thus use a linear fit to extrapolate the value of the carrier density in these regions. We can note that the carrier density is of order 10^{12} cm^{-2} which is a very low density. Most metals have carrier densities around 10^{23} cm^{-3} for instance. (Remark : At magic angle, twisted bilayer graphene becomes the most dilute superconductor, meaning with the lowest carrier density). This is particularly useful in our study as we showed in Sec.2.1.2 that the observation of a quadratic in temperature resistivity in a metal is favored by low electronic densities.

From the carrier density at full filling n_f we can then estimate the twist angle (in the small angle approximation).

$$n_f = \frac{8\theta^2}{\sqrt{3}a^2} \quad (7)$$

with a the lattice constant of graphene and θ the twist angle, we find for this device a twist angle of $1.35 \pm 0.03^\circ$

5.3 Study of the Hall angle in twisted bilayer graphene

Studying the temperature dependence of the longitudinal resistivity R_{xx} and of the Hall angle, defined by $\theta_H = \arctan \frac{R_{xy}}{R_{xx}}$ is a good way to check if our material can be described by Landau's theory of

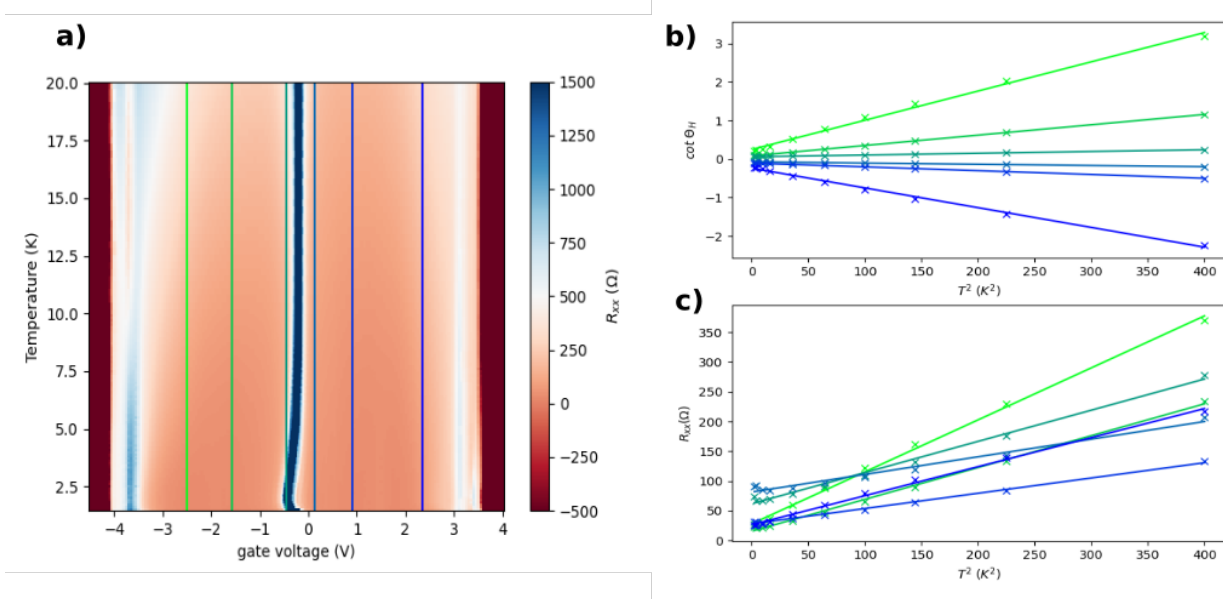


Figure 12: Temperature dependence of the Hall angle. a) n-T phase diagram, each vertical line correspond to a measurement of the Hall angle as a function of temperature b) Corresponding measurements of the cotangent of the Hall angle as a function of T^2 c) and of R_{xx} , both with field at 0.48 T for a device at 1.33° .

Fermi liquids.

Within the Fermi liquid theory, we expect the hall resistivity R_{xy} to be nearly independent of temperature. We thus expect that the Hall angle and R_{xx} have the same temperature dependence [26]. Non-Fermi liquid behavior can be highlighted by deviation from this expected behavior as what has been reported in the superconducting copper oxides [27]. We see in Fig.12, that both $\cot \theta_H$ (taken here at $B=0.48T$, we measure at low field to avoid non linear effects of the magnetic field) and R_{xx} (taken at 0 field) have a quadratic temperature dependence for temperatures between 1.5K and 20K. For every filling factor but the band insulators and the charge neutrality point insulating state (where resistivity measurements become quite complicated), we see a clear quadratic dependence on the temperature.

This measurement also allows us to verify the expected quadratic temperature dependence of the longitudinal resistance for most carrier densities expected within Landau's theory.

On this device, which is slightly above magic angle, all of the properties of the device we observed can be explained within Boltzmann theory and more specifically the physics observed seem to follow quite well Landau's Fermi liquid theory. As explained in Sec.2.1.2, resistivity can be explained by several phenomenons within Fermi liquid theory, Umklapp scattering or interband exchange. However, Umklapp scattering is limited by a geometric condition. Umklapp scattering cannot explain this dependence for carrier densities below $n_l = 6.9 \times 10^{11} \text{ cm}^{-2}$, for the twist angle we measured in the previous section (See Sec.2.1.2 for details of the calculation). We thus wish to measure the temperature dependence of R_{xx} at zero field for carrier densities below n_l .

5.4 Quadratic temperature dependence of the longitudinal resistivity for low carrier densities.

Here we measured the longitudinal resistivity for low carrier densities, at 0 field, for temperatures between 1.5K and 20K. We measured for gate voltages corresponding to carrier densities of the order of $1 \times 10^{12} \text{ cm}^{-2}$ or lower, keeping in mind that we don't expect to have Umklapp scattering below $7 \times 10^{11} \text{ cm}^{-2}$.

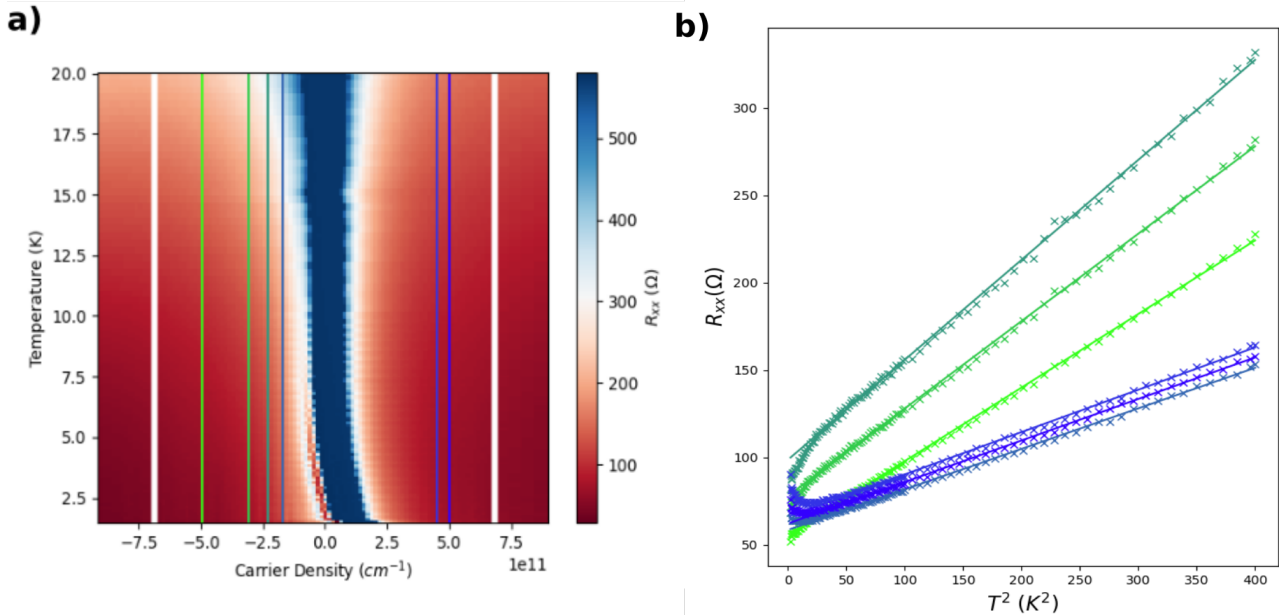


Figure 13: a) (n-T) Phase diagram of the device around charge neutrality, the white vertical lines correspond to the carrier density limits of Umklapp scattering b) Quadratic temperature dependence of R_{xx} near CNP without magnetic field for several carrier densities (highlighted in a)).

We observe a T^2 behavior for carrier densities below what is needed for Umklapp scattering. However as explained in the previous section, resistivity measurements close to the charge neutrality insulating state are hard to interpret. Besides, in order to calculate the limit n_l , we make assumptions of the shape of the Fermi surface. Indeed the calculations are made using the assumption that the Fermi surface is anisotropic. However, we still measure the T^2 behavior for carrier densities 4 times below the carrier density limit needed for Umklapp scattering. This questions the contribution of Umklapp scattering in the low temperature resistance of our device. We can interpret these results as evidence for Baber scattering rather than intraband Umklapp scattering which has been invoked in past studies [14], at least for lower carrier densities where we don't expect Umklapp scattering but still observe a quadratic dependence in temperature from the resistivity.

5.5 Metallic phase at "magic angle" in twisted bilayer graphene.

At magic angle, It is found that some phases cannot be described by the Fermi liquid picture. Indeed, close to the superconducting state, we observe a strange metal phase, the temperature dependence of the resistivity in this phase does not seem to correspond to the Fermi liquid theory. Here we report the measurement of a pair of contacts (on the same device previously studied) with a twist angle of approximately 1.18° (to approximate the twist angle, we used the same method as in Sec.5.2). In Fig.14 a) we can see new, more exotic phases arising compared to the pair of contacts studied in the previous sections. We see correlated insulating states at half filling (by measuring at lower temperatures we might expect to see superconductivity).

We measured the Hall angle at a carrier density of $n_s = -1.55 \times 10^{12} \text{ cm}^{-2}$ (where a strange metal phase was previously reported [13]). We observe (Fig.14 b)) a linear dependence of the longitudinal resistivity for temperatures down to 3 K, below the Bloch–Grüneisen temperature (equivalent of the Debye temperature for systems with small, anisotropic Fermi surfaces) of twisted bilayer graphene which is of the order of ten Kelvin [13]. Measurement of the cotangent of the Hall angle also differ from the expected behavior of a quadratic dependence, and of a similar dependence to the longitudinal resistivity. This indicates a deviation from the Fermi liquid behavior in this strongly correlated phase. The linear dependence seems to correspond well to the strange metal phase already measured in depth for magic angle (for similar twist angles and carrier density) in the group[13]. Such similar phases have

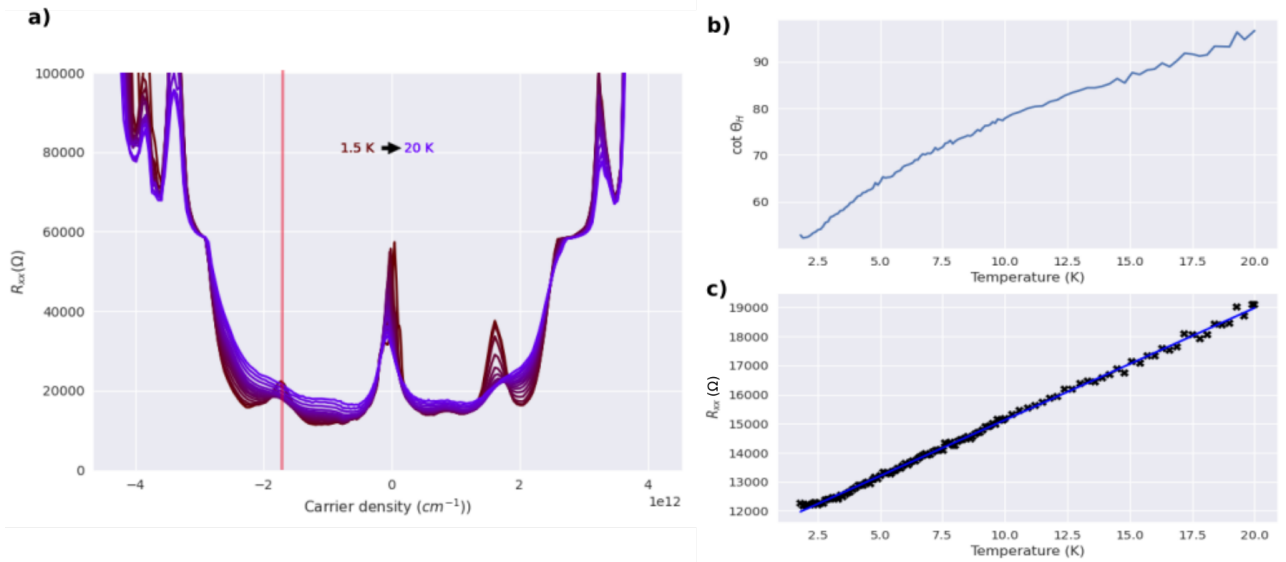


Figure 14: a) Resistivity as a function of electron doping for different temperatures ranging from 1.5K to 20K at $B = 0$ b) Temperature dependence of the Hall angle at $B = 0.5$ T and of c) the longitudinal resistivity for a carrier density of 1.55×10^{12} cm^{-2}

also been observed in many copper oxides [27].

6 Conclusion

In this report, we were able, thanks to the flatness of the electronic band and to the diluteness of the material, to study the Fermi liquid behavior of twisted bilayer graphene. We were able to question the scattering behavior behind low-temperature resistivity of the material by measuring electrical transport outside of the conceptual limits of Umklapp scattering. Finally, we briefly studied twisted bilayer graphene at its magic angle where novel phases arise, phases which deviate from the expected Fermi liquid behavior, namely the strange metallic phase.

During this internship, I was able to discover many aspects of the physics of 2D Materials and of the physics of strongly correlated electrons, from device fabrication (exfoliation, stacking), to characterisation of materials with Raman Spectroscopy or Atomic Force Microscopy, and finally device measurements by operating transport measurements at low temperature on a twisted bilayer graphene device.

Bibliography

- [1] K. S. Novoselov, A. K. Geim, S. V. Morozov, D. Jiang, Y. Zhang, S. V. Dubonos, I. V. Grigorieva, and A. A. Firsov. Electric field in atomically thin carbon films. *Science*, 306(5696):666–669, October 2004. Publisher: American Association for the Advancement of Science (A A A S).
- [2] Andres Castellanos-Gomez, Michele Buscema, Rianda Molenaar, Vibhor Singh, Laurens Janssen, Herre S J Van Der Zant, and Gary A Steele. Deterministic transfer of two-dimensional materials by all-dry viscoelastic stamping. *2D Materials*, 1(1):011002, April 2014.
- [3] Yuan Huang, Eli Sutter, Norman N. Shi, Jiabao Zheng, Tianzhong Yang, Dirk Englund, Hong-Jun Gao, and Peter Sutter. Reliable Exfoliation of Large-Area High-Quality Flakes of Graphene and Other Two-Dimensional Materials. *ACS Nano*, 9(11):10612–10620, November 2015.
- [4] Eva Y. Andrei and Allan H. MacDonald. Graphene bilayers with a twist. *Nature Materials*, 19(12):1265–1275, December 2020.
- [5] Yuan Cao, Valla Fatemi, Shiang Fang, Kenji Watanabe, Takashi Taniguchi, Efthimios Kaxiras, and Pablo Jarillo-Herrero. Unconventional superconductivity in magic-angle graphene superlattices. *Nature*, 556(7699):43–50, April 2018.
- [6] Mildred Dresselhaus, Gene Dresselhaus, Stephen B. Cronin, and Antonio Gomes Souza Filho. Electron and Phonon Scattering. In Mildred Dresselhaus, Gene Dresselhaus, Stephen Cronin, and Antonio Gomes Souza Filho, editors, *Solid State Properties: From Bulk to Nano*, Graduate Texts in Physics, pages 185–209. Springer, Berlin, Heidelberg, 2018.
- [7] Michael Kinza. Theory of Fermi-Liquids in Metals. In Michael Kinza, editor, *Theory of Fermi-liquids in Metals: A Compact Overview as an Introduction to Theoretical Solid-State Physics*, essentials, pages 1–29. Springer Fachmedien, Wiesbaden, 2021.
- [8] Dmitri Maslov. Transport in correlated electron systems i: Fermi liquids, August 2018.
- [9] Xiao Lin, Benoît Fauqué, and Kamran Behnia. Scalable T^2 resistivity in a small single-component Fermi surface. *Science*, 349(6251):945–948, August 2015.
- [10] W.G. Baber. The contribution to the electrical resistance of metals from collisions between electrons. *Proceedings of the Royal Society of London. Series A - Mathematical and Physical Sciences*, 158(894):383–396, January 1937.
- [11] Yuan Cao, Valla Fatemi, Ahmet Demir, Shiang Fang, Spencer L. Tomarken, Jason Y. Luo, J. D. Sanchez-Yamagishi, K. Watanabe, T. Taniguchi, E. Kaxiras, R. C. Ashoori, and P. Jarillo-Herrero. Correlated Insulator Behaviour at Half-Filling in Magic Angle Graphene Superlattices. *Nature*, 556(7699):80–84, April 2018. arXiv:1802.00553 [cond-mat].
- [12] A. H. Castro Neto, F. Guinea, N. M. R. Peres, K. S. Novoselov, and A. K. Geim. The electronic properties of graphene. *Reviews of Modern Physics*, 81(1):109–162, January 2009.
- [13] Alexandre Jaoui, Ipsita Das, Giorgio Di Battista, Jaime Díez-Mérida, Xiaobo Lu, Kenji Watanabe, Takashi Taniguchi, Hiroaki Ishizuka, Leonid Levitov, and Dmitri K. Efetov. Quantum critical behaviour in magic-angle twisted bilayer graphene. *Nature Physics*, 18(6):633–638, June 2022.
- [14] J. R. Wallbank, R. Krishna Kumar, M. Holwill, Z. Wang, G. H. Auton, J. Birkbeck, A. Mishchenko, L. A. Ponomarenko, K. Watanabe, T. Taniguchi, K. S. Novoselov, I. L. Aleiner, A. K. Geim, and V. I. Fal’ko. Excess resistivity in graphene superlattices caused by umklapp electron–electron scattering. *Nature Physics*, 15(1):32–36, January 2019.

- [15] Zhi-Da Song and B. Andrei Bernevig. Magic-Angle Twisted Bilayer Graphene as a Topological Heavy Fermion Problem. *Physical Review Letters*, 129(4):047601, July 2022. Publisher: American Physical Society.
- [16] Shin-ichi Uchida. Copper Oxide Superconductors. In Shin-ichi Uchida, editor, *High Temperature Superconductivity: The Road to Higher Critical Temperature*, Springer Series in Materials Science, pages 23–59. Springer Japan, Tokyo, 2015.
- [17] C. R. Dean, A. F. Young, I. Meric, C. Lee, L. Wang, S. Sorgenfrei, K. Watanabe, T. Taniguchi, P. Kim, K. L. Shepard, and J. Hone. Boron nitride substrates for high-quality graphene electronics. *Nature Nanotechnology*, 5(10):722–726, October 2010.
- [18] Sami Ullah, Xiaoqin Yang, Huy Q. Ta, Maria Hasan, Alicja Bachmatiuk, Klaudia Tokarska, Barbara Trzebicka, Lei Fu, and Mark H. Rummeli. Graphene transfer methods: A review. *Nano Research*, 14(11):3756–3772, November 2021.
- [19] Miho Arai, Satoru Masubuchi, Kenji Nose, Yoshitaka Mitsuda, and Tomoki Machida. Fabrication of 10-nm-scale nanoconstrictions in graphene using atomic force microscopy-based local anodic oxidation lithography. *Japanese Journal of Applied Physics*, 54(4S):04DJ06, March 2015. Publisher: IOP Publishing.
- [20] Andrea C. Ferrari and Denis M. Basko. Raman spectroscopy as a versatile tool for studying the properties of graphene. *Nature Nanotechnology*, 8(4):235–246, April 2013.
- [21] Yufeng Hao, Yingying Wang, Lei Wang, Zhenhua Ni, Ziqian Wang, Rui Wang, Chee Keong Koo, Zexiang Shen, and John T. L. Thong. Probing Layer Number and Stacking Order of Few-Layer Graphene by Raman Spectroscopy. *Small*, 6(2):195–200, January 2010.
- [22] C. Neumann, S. Reichardt, P. Venezuela, M. Drögeler, L. Banszerus, M. Schmitz, K. Watanabe, T. Taniguchi, F. Mauri, B. Beschoten, S. V. Rotkin, and C. Stampfer. Raman spectroscopy as probe of nanometre-scale strain variations in graphene. *Nature Communications*, 6(1):8429, September 2015.
- [23] Yucheng Lan, Mobolaji Zondode, Hua Deng, Jia-An Yan, Marieme Ndaw, Abdellah Lisfi, Chundong Wang, and Yong-Le Pan. Basic Concepts and Recent Advances of Crystallographic Orientation Determination of Graphene by Raman Spectroscopy. *Crystals*, 8(10):375, September 2018.
- [24] Haoxin Zhou, Tian Xie, Takashi Taniguchi, Kenji Watanabe, and Andrea F. Young. Superconductivity in rhombohedral trilayer graphene. *Nature*, 598(7881):434–438, October 2021.
- [25] Peter Jonathan Eaton and Paul West. *Atomic force microscopy*. Oxford University Press, Oxford ; New York, 2010. OCLC: ocn455831540.
- [26] A. Pippard. Magnetoresistance in metals. In *Magnetoresistance in metals*, 1989.
- [27] Jie Yuan, Qihong Chen, and Zhongxian Zhao. Scaling of the strange-metal scattering in unconventional superconductors. *Nature*, 602(7897):431–436, February 2022. Number: 7897 Publisher: Nature Publishing Group.